Journal of Computational Physics 438 (2021) 110366

Contents lists available at ScienceDirect

Journal of Computational Physics

www.elsevier.com/locate/jcp

# Limitations of stationary Vlasov-Poisson solvers in probe theory

L. Chiabó *, G. Sánchez-Arriaga

*Bioengineering and Aerospace Engineering Department, Universidad Carlos III de Madrid, Leganés, Madrid, 28911, Spain*

ARTICLE INFO

*Article history:*
Available online 20 April 2021

*Keywords:*
Vlasov equation
Computational plasma physics
Probe theory

ABSTRACT

Physical and numerical limitations of stationary Vlasov-Poisson solvers based on backward Liouville methods are investigated with five solvers that combine different meshes, numerical integrators, and electric field interpolation schemes. Since some of the limitations arise when moving from an integrable to a non-integrable configuration, an elliptical Langmuir probe immersed in a Maxwellian plasma was considered and the eccentricity ($e_p$) of its cross-section used as integrability-breaking parameter. In the cylindrical case, $e_p = 0$, the energy and angular momentum are both conserved. The trajectories of the charged particles are regular and the boundaries that separate trapped from non-trapped particles in phase space are smooth curves. However, their computation has to be done carefully because, albeit small, the intrinsic numerical errors of some solvers break these conservation laws. It is shown that an optimum exists for the number of loops around the probe that the solvers need to classify a particle trajectory as trapped. For $e_p \neq 0$, the angular momentum is not conserved and particle dynamics in phase space is a mix of regular and chaotic orbits. The distribution function is filamented and the boundaries that separate trapped from non-trapped particles in phase space have a fractal geometry. The results were used to make a list of recommendations for the practical implementation of stationary Vlasov-Poisson solvers in a wide range of physical scenarios.


## 1. Introduction

Grid-based Eulerian Vlasov and gyrokinetic solvers have been used to study many relevant scenarios in plasma physics, like laser-plasma interaction [1,2], plasma instabilities [3,4], plasma sheaths [5], magnetic nozzles [6], Landau damping [7], and tokamak plasmas [8] (find reviews in Refs. [9,10]). As opposed to particle methods, Eulerian solvers avoid the (macro-) particle noise by discretizing the distribution function in phase space. However, and besides the high computational cost, Eulerian solvers exhibit some undesired phenomena that can be classified into two categories. On one hand, one finds purely numerical issues like the violation of conservation laws, the generation of negative values of the distribution function, and recurrence effects. Numerical algorithms have been developed in the last few decades to avoid them [11–15]. On the other hand, there are real physical effects that jeopardize the numerical stability and/or the quality of the numerical solution. The most common phenomenon in this category is the filamentation of the distribution function, which is a physical mechanism that is consequence of the free-streaming character of the equation that governs its evolution. It creates structures at a small

* Corresponding author.
*E-mail addresses:* lchiabo@pa.uc3m.es (L. Chiabó), gonzalo.sanchez@uc3m.es (G. Sánchez-Arriaga).

https://doi.org/10.1016/j.jcp.2021.110366

scale in phase space, strong gradients, and finally un-physical numerical instabilities. Artificial dissipation, smoothing, and filtration are common techniques to avoid this problem [7,11,16].

Langmuir and emissive probes, which are the oldest diagnostic devices for low-temperature plasmas, have also been investigated with Eulerian codes. The sheath formation around planar and cylindrical probe was studied in the framework of the non-stationary Vlasov-Poisson system with Eulerian solvers [17–20]. These solvers play an important role in the understanding of basic phenomena, like the particle trapping during the transient phase [19,20], but their use for constructing databases with current-voltage characteristics (I-V curves) in a broad range of physical parameters is beyond actual computational capabilities. For this reason, present models for the I-V curves in collisionless plasmas come from analytical and numerical analysis of the stationary Vlasov-Poisson system. Probe community usually refers to it as Orbital Motion Theory (OMT) [21–25]. OMT finds the value of the distribution function at every point in real and velocity space by taking advantage of the existence of conserved quantities. An analysis of the particle orbits, which coincide with the characteristics of the Vlasov equation, allows to write the density of the species as a function of the electrostatic potential. Its substitution in Poisson equation yields to an integro-differential equation. Its solutions have been found by using perturbation techniques when a small physical parameter exists, and with iterative numerical algorithms otherwise. For instance, in the case of cylindrical Langmuir and emissive probes immersed in collisionless plasmas, the energy, the angular momentum, and the distribution function along the characteristics of Vlasov equations are all conserved and I-V curves have been found for a broad range of conditions [24,26,27].

The analysis of physical scenarios without enough conserved quantities, i.e. non-integrable configurations, is more delicate. The trajectories have to be found by numerical integration and chaotic and regular orbits may coexist. Some examples are tape-like probes at rest and cylindrical probes immersed in flowing plasmas, which do not conserve the angular momentum along the trajectories of the particles. Some authors implemented *backward* and *forward* Liouville methods [26,28], that take advantage of the collisionless character of the plasma and the conservation of the distribution function along the characteristic equations. In the backward Liouville method, and for a given electrostatic potential, the value of the distribution function at each point of the space-velocity mesh is found by integrating numerically the characteristic equations backward in time until the orbit hits a boundary where the value of the distribution function is known (e.g., the probe or the outer boundary of the computational domain). The Poisson equation is then used to find a new electrostatic potential and an iterative process is implemented until a self-consistent solution is found. This approach provides a detailed and rigorous description and, unlike particle-in-cell codes, it is free of statistical error [29].

This work discusses the limits of stationary Vlasov-Poisson (VP) solvers based on backward Liouville methods. It uncovers some numerical and physical phenomena that may explain the lack of convergence found in a previous work [26] and should be considered during the practical implementation of these solvers. In particular, it analyzes the transition from regular to chaotic dynamics of the trapped particle population when the integrability of the orbits is broken due to a lack of conserved quantities. Although the results are general and can be applied to a broad range of physical scenarios, we illustrate them by considering a Langmuir probe with elliptical cross-section. Such scenario is very convenient to test VP solvers because the eccentricity of the probe acts as integrability-breaking parameter and, for zero eccentricity, there are solutions that can be used to benchmark the solvers [24]. Furthermore, it is a relevant problem in several areas, including probe theory, spacecraft charging, and dusty plasmas. Next section presents the hypotheses of the model and the numerical algorithms used to solve the Vlasov-Poisson system. Sections 3 and 4 show the numerical and physical limits of stationary Vlasov solvers. These results are used to prepare a list of recommendations for the practical implementation of stationary Vlasov-Poisson solvers. A discussion of the results and the conclusions are presented in Sec. 5.

## 2. Stationary Vlasov-Poisson solvers

### 2.1. Description of the algorithms

A wide variety of interesting scenarios involves an object with contour $\Gamma$ immersed in a collisionless, unmagnetized, and Maxwellian plasma. Let us assume that $N_0$ is the unperturbed plasma density and $T_{0\alpha}$ are the temperatures of the electrons ($\alpha = e$) and the ions ($\alpha = i$). In stationary conditions, their distribution functions $f_\alpha(\boldsymbol{r}, \boldsymbol{v})$ and the electrostatic potential $\phi$ are governed by the stationary Vlasov-Poisson system

$$\boldsymbol{v} \cdot \nabla_{\boldsymbol{r}} f_\alpha + \frac{e_\alpha}{\delta_\alpha} \boldsymbol{E} \cdot \nabla_{\boldsymbol{v}} f_\alpha = 0, \tag{1a}$$

$$\Delta\phi = n_e - e_i n_i, \tag{1b}$$

where the densities of the species and the electric field are found from

$$n_\alpha(\boldsymbol{r}) = \int f_\alpha(\boldsymbol{r}, \boldsymbol{v}) d\boldsymbol{v}. \tag{2}$$

$$\boldsymbol{E} = -\nabla\phi \tag{3}$$

In Eqs. (1a)-(3), the distribution functions ($f_\alpha$), the electrostatic potential ($\phi$), the densities ($n_\alpha$), the position vector ($\boldsymbol{r}$), the velocity vector ($\boldsymbol{v}$), and the electric field ($\boldsymbol{E}$) are normalized over $m_\alpha N_0/k_B T_{\alpha 0}$, $k_B T_{e0}/e$, $N_0$, the electron Debye

length $\lambda_{De} \equiv \sqrt{\epsilon_0 k_B T_{e0}/e^2 N_0}$, the thermal velocities $v_{th\alpha} \equiv \sqrt{k_B T_{\alpha 0}/m_\alpha}$, and $\sqrt{k_B T_{e0} N_0/\epsilon_0}$, respectively. Here $m_\alpha$ are the masses of the plasma species, $k_B$ the Boltzmann constant, $\epsilon_0$ the vacuum permittivity and $e$ the elementary charge. We also introduced the dimensionless parameters:

$$e_\alpha \equiv q_\alpha/e, \quad \delta_\alpha \equiv T_{\alpha 0}/T_{e0}, \tag{4}$$

where $q_\alpha$ are the charges of the particles. The boundary conditions of Eqs. (1a), (1b) at $\Gamma$ and $r \to \infty$, which depend on the particular physical configuration, are explained in Sec. 2.2.

Stationary solvers based on backward Liouville methods find numerical solutions of Eqs. (1a)-(1b) as follows. A computational domain, bounded by the contour of the object $\Gamma$ and the external boundary $\Omega_{max}$, is discretized by using $N$ nodes. As explained in Appendix A.1, this work considers three meshes in a 2-dimensional configuration: (i) unstructured mesh of $N$ nodes with Cartesian coordinates $(x_i, y_i)$, (ii) structured cylindrical mesh with $N = N_r \times N_\theta$ nodes of coordinates $(r_i, \theta_i)$, where $r$ and $\theta$ are the radial distance and the azimuthal angle, and (iii) structured elliptic mesh with $N = N_\xi \times N_\eta$ nodes of elliptic coordinates $(\xi_i, \eta_i)$. The unknowns of the algorithm are the values of the charge density at the nodes. They are gathered into vector $\boldsymbol{\rho} \equiv e_i \boldsymbol{n}_i - \boldsymbol{n}_e \in \mathcal{R}^N$, which involves the corresponding density vectors. The structure of the plasma sheath is found by looking for the value of $\boldsymbol{\rho}$ that satisfies the following set of nonlinear algebraic equations (see for instance Ref. [26] and therein)

$$\boldsymbol{F}(\boldsymbol{\rho}) \equiv \boldsymbol{\rho} - \mathcal{V}[\mathcal{P}(\boldsymbol{\rho})] = 0, \tag{5}$$

where $\mathcal{V}$ and $\mathcal{P}$ are operators (solvers) of the Vlasov and Poisson equations, respectively. Given an initial guess $\boldsymbol{\rho}_0$, a Newton-Raphson method [30] can find the solution of Eq. (5) by implementing the map

$$\boldsymbol{\rho}_{n+1} = \boldsymbol{\rho}_n - \boldsymbol{J}^{-1}|_{\boldsymbol{\rho}_n} \boldsymbol{F}(\boldsymbol{\rho}_n), \quad n = 0, 1, \ldots \tag{6}$$

with $\boldsymbol{J}|_{\boldsymbol{\rho}_n}$ the Jacobian matrix of $\boldsymbol{F}$ evaluated at $\boldsymbol{\rho}_n$. In our implementation, this matrix is computed with a central finite difference scheme and the iteration is stopped when the Euclidean norm of the error function $\boldsymbol{F}$ is below a tolerance $\epsilon_{tol}$, $\|\boldsymbol{F}\|_2 < \epsilon_{tol}$.

The Poisson solver $\mathcal{P}$ is a discrete version of Eq. (1b). It receives vector $\boldsymbol{\rho}$ and finds a vector with the values of the electrostatic potential at the nodes as

$$\boldsymbol{\phi} = \mathcal{P}(\boldsymbol{\rho}) = \bar{\boldsymbol{A}}\boldsymbol{\rho} + \boldsymbol{\phi}_{BC}, \tag{7}$$

where matrix $\bar{\boldsymbol{A}} \in \mathcal{R}^{N \times N}$ and vector $\boldsymbol{\phi}_{BC} \in \mathcal{R}^N$ depend on the mesh and the boundary conditions, i.e. the value of $\phi$ at $\Gamma$ and at the unperturbed plasma boundary $\Omega_{max}$. Two Poisson solvers are considered in this work: (i) a finite element-based solver for the unstructured mesh, and (ii) a finite difference-based solver for the two structured meshes. More details and references on the computation of $\bar{\boldsymbol{A}}$ and $\boldsymbol{\phi}_{BC}$ for these two solvers are given in Appendix A.2.

The Vlasov solver receives the electrostatic potential and computes the distribution functions that are consistent with Eq. (1a). Our solver is based on a backward Liouville algorithm that takes advantage of the collisionless character of the plasma. Equation (1a) can also be written as $df_\alpha(r, \theta, v_r, v_\theta)/d\tau = 0$ and $f_\alpha$ is conserved along the characteristics

$$\frac{d\boldsymbol{r}}{d\tau} = \boldsymbol{v} \tag{8}$$

$$\frac{d\boldsymbol{v}}{d\tau} = -\frac{e_\alpha}{\delta_\alpha}\nabla\phi \tag{9}$$

where $\tau$ parametrizes the integral curves. These equations coincide with the equations of motion of the charged particles and $\tau$ can be interpreted as a dimensionless time. The value of $f_\alpha$ at $\boldsymbol{x}_{s0} \equiv (\boldsymbol{r}_0, \boldsymbol{v}_0)$ is found by integrating Eqs. (8)-(9) numerically backward in time with initial conditions $\boldsymbol{x}_{s0}$ up to a time $\tau_f$, when the trajectory hits a boundary of the computational domain at $\boldsymbol{x}_{sf} \equiv (\boldsymbol{r}_f, \ \boldsymbol{v}_f)$. Three numerical integrators are discussed in this work: (i) a Runge-Kutta scheme, (ii) a Leapfrog (symplectic) scheme, and (iii) an energy-conserving Crank-Nicolson scheme [31]. Different methods are used to reconstruct the electric field from the electrostatic potential at the nodes of the mesh (find details of the algorithms in Appendix A.3). Since $f_\alpha$ is conserved, one has $f_\alpha(\boldsymbol{x}_{s0}) = f_\alpha(\boldsymbol{x}_{sf})$, with $f_\alpha(\boldsymbol{x}_{sf})$ given by the boundary conditions. If the trajectory $\boldsymbol{x}_s(\tau)$ does not hit any boundary after performing $N_{tr}$ loops around the probe, then the particle is considered as trapped and we set $f_\alpha(\boldsymbol{x}_{s0}) = 0$. Fig. 1 shows examples of these trajectories around an elliptic probe. They all have $(x_0, y_0) = (3.5, 0)$ and, depending on the initial value of the velocity vector, the trajectory hits the outer boundary (A), the probe (B), or is trapped (C). Once the distribution functions are known, the densities at the nodes are obtained from Eq. (2) and the charge density vector from $\boldsymbol{\rho} = e_i \boldsymbol{n}_i - \boldsymbol{n}_e$.

The numerical integration of the trajectories, i.e. the Vlasov solver, is the most demanding part of the algorithm from a computation standpoint. It can be avoided if the characteristic equations admit two constants of motion, thus making the system integrable. Interestingly, Eqs. (8)-(9) are a Hamiltonian system with Hamiltonian

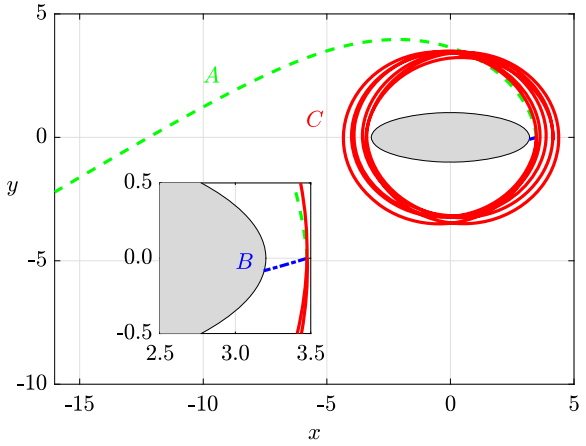


**Fig. 1.** Example of trajectories that hit the outer boundary (A), the probe (B), and are trapped (C).

**Table 1**
Characteristics of the five algorithms. FEM and FDM denote finite element and finite difference methods. More details are given in Appendix A.

| Name | Mesh | Poisson solver | Integrator | $\boldsymbol{E}$ reconstruction |
|---|---|---|---|---|
| FEM-RK | Unstructured | FEM [26] | Runge-Kutta [30] | Polynomial fitting + Natural neighbor interpolation [32] |
| FDM-RK | Structured | FDM | Runge-Kutta [30] | FDM + Bilinear interpolation [30] |
| FEM-LF | Unstructured | FEM [26] | Leapfrog [30] | Polynomial fitting + Natural neighbor interpolation [32] |
| FDM-LF | Structured | FDM | Leapfrog [30] | FDM + Bilinear interpolation [30] |
| FDM-CN | Structured | FDM | Crank-Nicolson [31] | B-spline [31] |

$$\mathcal{H}_\alpha(\boldsymbol{r},\boldsymbol{v}) = \frac{1}{2}v^2 + \frac{e_\alpha}{\delta_\alpha}\phi(\boldsymbol{r}). \tag{10}$$

Since the Hamiltonian is $\tau$-independent, $\mathcal{H}_\alpha$ is a constant of motion of Eqs. (8)-(9) (note that $\mathcal{H}_\alpha$ also coincides with the energy). Except for very special cases, a second constant of motion does not exist. Equations (8)-(9) are, in general, a non-integrable system and a mix of regular and chaotic orbits exists in phase space.

Table 1 summarizes the characteristics of the different Vlasov-Poisson solvers prepared in this work. They are named as FEM-RK, FDM-RK, FEM-LF, FDM-LF, and FDM-CN and combine different meshes, Poisson solvers, numerical integrators, and methods to reconstruct the electric field from the values of the electrostatic potential at the nodes of the mesh. As explained in the next section, a 2-dimensional Langmuir probe will be used as study case.

### 2.2. Langmuir probe with elliptic cross-section

We consider a 2-dimensional probe with an elliptic cross-section. It is centered at the origin of the frame of reference and its contour in cylindrical $(r,\theta)$ and elliptic $(\xi,\eta)$ coordinates read

$$\Gamma = \left\{(r,\theta) \;|\; r^2\left(\cos^2\theta + \frac{\sin^2\theta}{1-e_p^2}\right) = \frac{r_p^2}{1-e_p^2}\right\} = \left\{(\xi,\eta) \;|\; \xi = \xi_p \equiv \sinh^{-1}\left(\frac{\sqrt{1-e_p^2}}{e_p}\right)\right\}. \tag{11}$$

The ellipse is characterized by its semi-minor axis $r_p$ and its eccentricity $e_p$. Due to the symmetry of the ellipse, the following relations hold: $\phi(x,y) = \phi(-x,y)$, $\phi(x,y) = \phi(x,-y)$, $n_\alpha(x,y) = n_\alpha(-x,y)$ and $n_\alpha(x,y) = n_\alpha(x,-y)$. Therefore, we need to compute $\phi$ and $f_\alpha$ onto the first quadrant only. Unstructured and elliptic structured meshes for two elliptic probes with $e_p = 0.95$ and $r_p = 1$ are shown in the left and middle panels of Fig. 2. The right panel corresponds to a cylindrical probe with $r_p = 1$ and a structured cylindrical mesh. For the unstructured mesh and the structured mesh with cylindrical coordinates, the computational domain is bounded by $\Gamma$ and $\Omega_{max} = \{(r,\theta) \;|\; r = r_{max}\}$, whereas for the structural mesh with elliptic coordinates we use $\Gamma$ and $\Omega_{max} = \{(\xi,\eta) \;|\; \xi = \xi_{max}\}$. Here $r_{max}$ and $\xi_{max}$ are two numerical parameters that should be selected large enough to recover plasma quasi-neutrality.

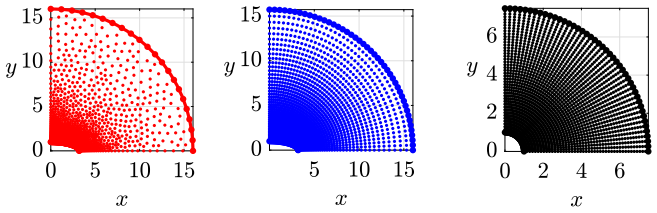


**Fig. 2.** Examples of computational domains and meshes for elliptical and cylindrical probes.

Regarding the Vlasov solver, the conservation of $\mathcal{H}_\alpha$ and the particular shape of $\Gamma$ suggest to make a change of variables. For each node $\boldsymbol{r}_i$, instead of the Cartesian $(v_x, v_y)$ or polar $(v_r, v_\theta)$ velocity components, we consider $f_\alpha(\boldsymbol{r}_i, \mathcal{H}_\alpha, \zeta)$, with $\mathcal{H}_\alpha$ given in Eq. (10) and angle $\zeta \in [0\ 2\pi]$ defined as

$$\zeta \equiv \tan^{-1}\left(\frac{\boldsymbol{v}\cdot\boldsymbol{t}}{\boldsymbol{v}\cdot\boldsymbol{n}}\right), \tag{12}$$

where $\boldsymbol{t}$ is the unit vector tangent to the ellipse passing through node $\boldsymbol{r}_i$ and confocal with $\Gamma$ and $\boldsymbol{n}$ the normal unit vector in the outward direction. For each node $\boldsymbol{r}_i$, the Vlasov solver defines a mesh in the $\mathcal{H}_\alpha - \zeta$ plane with $N_\mathcal{H} \times N_\zeta$ nodes. Along the $\zeta$-axis, the algorithm takes $N_\zeta$ non-uniformly distributed nodes $\zeta_j$ within the interval $[0,\ 2\pi]$, with a higher resolution in the proximity of the limits of the interval. Regarding the $\mathcal{H}_\alpha$-axis, in principle one should consider the semi-infinite domain $[0,\ \infty)$. However, according to Eq. (10), the Hamiltonian has to be larger than or equal to $\mathcal{H}^\alpha_{min} \equiv max\{0, e_\alpha\phi(\boldsymbol{r})/\delta_\alpha\}$. Moreover, the numerical algorithm truncates the semi-infinite domain and takes $\mathcal{H}^\alpha_{min} \leq \mathcal{H}_\alpha \leq \mathcal{H}^\alpha_{max}$, with $\mathcal{H}^\alpha_{max}$ a large enough numerical parameter. The $\mathcal{H}_\alpha$-mesh, with nodes $\mathcal{H}_{\alpha,k}$ and $k = 1 \ldots N_\mathcal{H}$, is not uniform and a higher density of nodes is taken close to $\mathcal{H}^\alpha_{min}$. The value of $f_\alpha$ at every node of the four-dimensional mesh $(\boldsymbol{r}_i, \mathcal{H}_\alpha, \zeta)$ is found with the backward Liouville algorithm explained in Sec. 2.1. The boundary conditions of the Vlasov solver are

$$f_\alpha(\Gamma, \mathcal{H}_\alpha, -\frac{\pi}{2} < \zeta < \frac{\pi}{2}) = 0, \tag{13a}$$

$$f_\alpha(\Omega_{max}, \mathcal{H}_\alpha, \zeta) = \frac{\exp(-\mathcal{H}_\alpha)}{\pi}, \tag{13b}$$

which corresponds to a non-emitting probe (Eq. (13a)) immersed in a Maxwellian plasma (Eq. (13b)). The densities at the nodes of the mesh are found from Eq. (2) that now reads

$$n_\alpha(\boldsymbol{r}) \approx \frac{1}{2}\int_{\mathcal{H}^\alpha_{min}}^{\mathcal{H}^\alpha_{max}}\int_0^{2\pi} f_\alpha(\boldsymbol{r}, \mathcal{H}_\alpha, \zeta)\, d\mathcal{H}_\alpha d\zeta, \tag{14}$$

being the factor 1/2 the jacobian of the transformation $\boldsymbol{v} \to (\mathcal{H}_\alpha, \zeta)$. These integrals were computed with a trapezoidal method

$$n_\alpha(\boldsymbol{r}_i) \approx \frac{1}{2}\sum_{j=2}^{N_\zeta} \frac{I_\alpha(\boldsymbol{r}_i, \zeta_j) + I_\alpha(\boldsymbol{r}_i, \zeta_{j-1})}{2}(\zeta_j - \zeta_{j-1}), \tag{15a}$$

$$I_\alpha(\boldsymbol{r}_i, \zeta_j) \approx \sum_{k=2}^{N_\mathcal{H}} \frac{f_\alpha(\boldsymbol{r}_i, \mathcal{H}_{\alpha,k}, \zeta_j) + f_\alpha(\boldsymbol{r}_i, \mathcal{H}_{\alpha,k-1}, \zeta_j)}{2}(\mathcal{H}_{\alpha,k} - \mathcal{H}_{\alpha,k-1}). \tag{15b}$$

Several tests were carried out to verify the correct implementation of the algorithms. First, the Poisson solver and the electric field reconstruction algorithms were checked with some analytical solutions and test functions. Second, the three Vlasov-Poisson solvers of Table 1 were verified by setting $e_p = 0$ (round probe) and comparing the results with the solutions of Ref. [27] without electron emission. For $e_p = 0$, angle $\theta$ is a cyclic variable of the Hamiltonian in Eq. (10), i.e. $\partial\mathcal{H}/\partial\theta = 0$, and the angular momentum $p_\theta = r v_\theta$ is conserved. Since for that case $\mathcal{H}$ and $p_\theta$ are conserved, the Vlasov-Poisson system can be written as a single integro-differential equation [27] and it is an excellent benchmark case to test our solvers. Finally, for $e_p > 0$, we compared the three solvers among them and checked that they provide similar solutions (up to the errors and differences discussed in Sec. 3).

Hereafter, we set the physical parameters

$$\phi_p = -4, \quad e_i = 1, \quad e_e = -1, \quad \delta_i = 1, \quad r_p = 1 \tag{16}$$

and consider different values of eccentricities $e_p$. For all the configurations presented in this work, we used the following set of numerical parameters

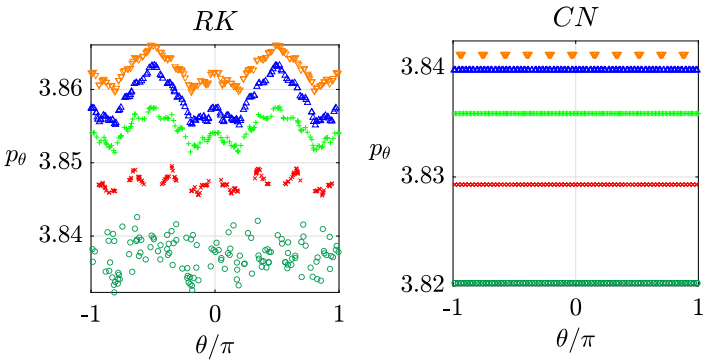


**Fig. 3.** Poincaré section ($v_r = 0$ plane) of 5 trapped ions moving around a cylindrical probe and with initial conditions $(x_0, y_0, \mathcal{H}_i) = (3.05, 0, 0.505)$ and different velocity angles $\zeta_0$, identified by different colors and markers. Left and right panels were obtained with RK and CN Vlasov solvers. (For interpretation of the colors in the figure(s), the reader is referred to the web version of this article.)

$$N_\zeta = 360, \quad N_{\mathcal{H}} = 300, \quad \mathcal{H}^e_{max} = \mathcal{H}^e_{min} + 6.0, \quad \mathcal{H}^i_{max} = 6.0. \tag{17}$$

When we studied cylindrical probes, we set $r_{max} = 7.5$ and used $N = 1893$ and $N_r \times N_\theta = 45 \times 45$ for the unstructured mesh and the structured (cylindrical) mesh, respectively. For elliptic probes, we set $r_{max} = 16$ and $N = 1898$ for the unstructured mesh and $\xi_{max} \approx 7.26\xi_p$ and $N_\xi \times N_\eta = 45 \times 45$ for the structured (elliptic) mesh.

## 3. Numerical limitations

This section and the next one discuss some limitations and interesting phenomena arising in stationary VP solvers based on backward Liouville methods. For convenience, we classify them into numerical and physical. We investigate both integrable and non-integrable scenarios by considering cylindrical ($e_p = 0$) and elliptical ($e_p \neq 0$) probes, respectively.

### 3.1. The breaking of conservation laws

Equations (8)-(9) conserve the Hamiltonian $\mathcal{H}_\alpha$ and, for $e_p = 0$, the angular momentum $p_\theta = rv_\theta$. However, their numerical integration does not preserve, in general, these two invariants due to inherent numerical errors of the algorithm. They include discretization, interpolation, and integration errors. The inaccuracies, which are small for a good setup of the numerical parameters, are not important for most of the orbits that hit the outer boundary of the computational domain or the probe. For these two types of trajectories, the corresponding integrations are typically short in time and the numerical errors just change slightly the impacting point and the Hamiltonian $\mathcal{H}_\alpha$ with respect to an error-free integration. Such a feature has a small effect on the final solution because the value of the distribution function is set to zero if the trajectory hits the probe independently of the impacting point and the Hamiltonian and, in case the trajectory hits the outer boundary, its value is slightly different according to Eq. (13b). However, for trapped particles, integrations last longer and orbits that should be trapped could hit the boundaries of the computational domain due to the accumulation of numerical error. The assigned value of the distribution function could incorrectly jump from zero to a finite value.

The performances of the numerical integrators were studied by using the potential profile obtained with the Vlasov-Poisson solver of Ref. [27] for a probe with $e_p = 0$ and the physical and numerical parameters of Eqs. (16)-(17). Left Panel in Fig. 3 shows the intersections with the $v_r = 0$ plane (Poincaré section) of five trajectories of trapped ions computed with the RK integrator and the unstructured mesh. They have the initial condition $(x_0, y_0, \mathcal{H}_i) = (3.05, 0, 0.505)$ and different values of $\zeta_0$. Although the potential profile satisfied $\partial\phi/\partial\theta = 0$, the small error in its reconstruction gives an electric field that does not respect strictly the axial-symmetry of the physical configuration. Consequently, $p_\theta = rv_\theta$ is not constant and exhibits variations of around 1%. The right panel, which shows the same result but computed with the CN algorithm and the cylindrical structured mesh, reveals that such algorithm is a better choice for this particular scenario and conserves the angular momentum of the trajectories around cylindrical probes.

Regarding the conservation of the Hamiltonian, it is even more delicate for the accurate computation of the trapped ions. This topic was investigated by finding the full solution of the Vlasov-Poisson system with the solvers, the parameters in Eqs. (16)-(17), $N_{tr} = 2$, and an elliptic probe with $e_p = 0.95$. Once the potential was found for each of the five solvers, we investigated the evolution of the error of the hamiltonian along the orbits of some trapped ions. In Fig. 4, the FEM-RK solver (red solid line, left panel) presents an error of almost 10%, and a secular variation. The result for the FDM-RK solver (black dash-dotted line, left panel), which exhibits an error below 3% and no secular variation, reveals that the use of a structured mesh and the bilinear interpolation for the reconstruction of the electric field outperforms the combination of an unstructured mesh with a natural neighbor interpolation. Similar results are found when the RK integrator is substituted by a (symplectic) second-order LeapFrog (LF) scheme (see right panel of Fig. 4). No significant improvement in the energy conservation was observed by decreasing the time step (not shown). Therefore, the algorithm that computes the electric

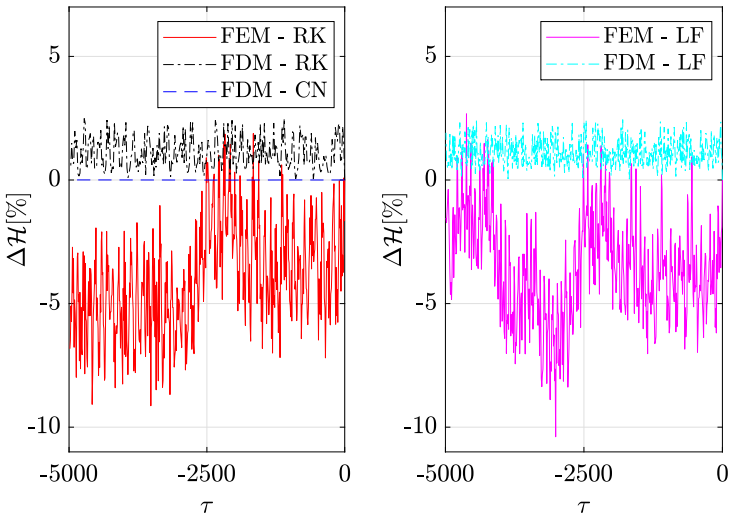


**Fig. 4.** Evolution of $\Delta\mathcal{H} = [\mathcal{H}(\tau) - \mathcal{H}(0)] \times 100/\mathcal{H}(0)$ for a trapped ion moving around an elliptical probe ($e_p = 0.95$). (For interpretation of the colors in the figure(s), the reader is referred to the web version of this article.)

field along the particle orbits from the value of the electrostatic potential at the nodes of the mesh is the main source of error. The FDM-CN solver (blue dashed line in the left panel), which is an implicit method, conserves the Hamiltonian up to the tolerance set to the Newton method implemented at every time step (equal to $10^{-8}$ in our calculations).

### 3.2. Trapping criterion

Stationary solvers neglect the contribution of the trapped population to $f_\alpha$. For a given initial condition, $\boldsymbol{x}_{s0}$, one sets $f_\alpha(\boldsymbol{x}_{s0}) = 0$ if the trajectory performs $N_{tr}$ loops around the probe without hitting any boundary of the computational domain. The solutions of the Vlasov-Poisson solvers are insensitive to numerical parameters (e.g., $N_\zeta, N_\mathcal{H}, \mathcal{H}_{max}$) if they are chosen beyond certain thresholds. However, as shown below, the role of $N_{tr}$ is slightly different and its selection involves subtler considerations related to the algorithms. This topic was investigated by first finding the electrostatic potential for a cylindrical probe ($e_p = 0$) with the algorithm of Ref. [27], and then analyzing in detail the influence of $N_{tr}$ on the structure of the ion distribution function calculated with our numerical integrators. The three top panels in Fig. 5 show the distribution function of the ions at point $(x, y) = (3.05, 0)$ for $N_{tr} = 1, 2$, and 10 computed with the RK solver and the unstructured mesh. For convenience, we used a high resolution grid of $N_\mathcal{H} = 100 \times N_\zeta = 250$ points in the region of the $\mathcal{H}_i - \zeta$ plane where trapped orbits exist. Black regions are initial conditions in velocity space that yield trajectories hitting the outer boundary of the computational box before performing $N_{tr}$ loops. For these values, the algorithm sets the value of the distribution function equal to the Maxwellian. For initial conditions in the orange region the trajectories perform $N_{tr}$ loops around the probe and the algorithm sets the value of the distribution function equal to zero. The red solid line is the boundary provided by the orbit analysis of Ref. [27], which takes advantage of the conservation of $\mathcal{H}_i$ and $p_\theta$ to find the exact result. If $N_{tr}$ is too low, for instance $N_{tr} = 1$ in the left panel, the algorithm incorrectly classifies some orbits as trapped and the ion density is underestimated. If $N_{tr}$ is very large (see $N_{tr} = 10$ in the top right panel) the computational cost is higher and some trajectories that should be trapped are incorrectly classified as non-trapped. Numerical errors, breaking the conservation of $\mathcal{H}_i$ and $p_\theta$ during the long integrations, make trapped orbits incorrectly hit the outer boundary of the computational domain. The ion density would be overestimated. Therefore, the study shows that choosing low values of $N_{tr}$, but above a reasonable threshold, has two advantages: higher accuracy and lower computational cost. Similar results are found for the CN solver (bottom panels), except that in this case the trapped particles close to the boundary are classified correctly even for large $N_{tr}$ values. This is a positive consequence of the energy conserving character of the algorithm. Nevertheless, since the computational cost of the three solvers depends on the choice of $N_{tr}$, it is recommendable to perform a sensitivity analysis of this parameter for each physical configuration.

## 4. Physical limitations

### 4.1. Trapped particles

An important limitation of stationary Vlasov (collisionless) solvers is their inability to compute the population of trapped particles. The most common strategy adopted in previous works, and also here, was neglecting it. However, this can lead to incorrect solutions. Since particles can be trapped due to collisions and/or during transient phases, studies in the framework

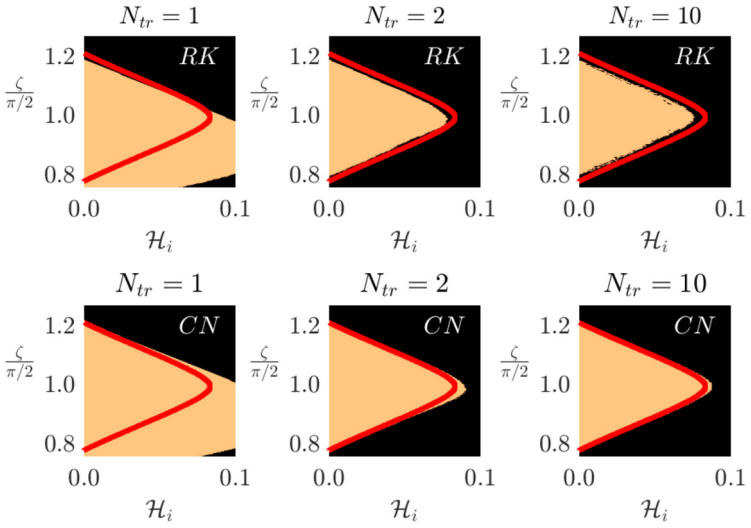


**Fig. 5.** Distribution function at $(x, y) = (3.05, 0)$ in the $\mathcal{H}_i - \zeta$ plane for different values of $N_{tr}$ obtained with the RK (top) and CN (bottom) solvers. Orange and black regions correspond to initial conditions yielding trajectories that are trapped and hit the unperturbed plasma boundary of the computational domain, respectively. The red line is the boundary obtained with the solver of Ref. [27]. Research data and post-processing scripts are available at the [dataset] [33]. (For interpretation of the colors in the figure(s), the reader is referred to the web version of this article.)

of the stationary Boltzmann equation system and/or the non-stationary Vlasov equation are needed. We identify and discuss below three scenarios.

First, there are configurations where, even neglecting the population of trapped particles, self-consistent solutions of the Vlasov-Poisson system can be found. The incorporation of trapped particles just impacts the profile of the electrostatic potential. An example that belongs to this category is a cylindrical Langmuir probe immersed at rest in a Maxwellian plasma, as corroborated by the comparison of steady-state solutions of the Vlasov-Poisson system without trapped particles [24] against solutions with trapped particles coming from stationary Boltzmann-Poisson [34] and non-stationary Vlasov-Poisson [19] systems. Second, there are physical scenarios where ignoring the population of trapped particles creates convergence issues in stationary Vlasov solvers. For instance, a plasma expansion in a slender magnetic nozzle exhibits this problem and, only after adding a heuristic population of trapped electrons, numerical solutions were found [35]. A later study with a non-stationary Vlasov solver showed that there are indeed trapped electrons [6], but they represent a much smaller fraction to the one considered in the stationary analysis. In the third scenario the population of trapped particles is a fundamental component of the solution. A positively polarized Langmuir probe immersed in a flowing plasma and mesothermal conditions, i.e. plasma velocity large (small) compared with ion (electron) thermal velocity, is a well-known archetype. Without trapping, the density of the electrons (attracted species) should be lower than $N_0$ [36] but the density of the hypersonic (repelled) ions should exceed $N_0$ in the front side, thus breaking the quasi-neutrality in a broad region. It was proposed [37], and later verified with non-stationary Vlasov simulations [20], that a population of trapped particles is indeed essential to recover the quasi-neutrality at the front.

### 4.2. Filamentation of the distribution function

For physical configurations without axial-symmetry, the angular momentum is not conserved. Equations (8)-(9) become a non-integrable system, and non-regular (chaotic) dynamics can appear. To illustrate the impact of this feature, we computed a solution of the Vlasov-Poisson system for an elliptic probe with $e_p = 0.95$, $N_{tr} = 2$, and the physical and numerical parameters of Sec. 2.2. We used the FDM-CN solver that, as shown in Sec. 3, is the best solver for this particular configuration. The electrostatic potential was used afterwards to study in detail the dynamics of the trapped ions. Fig. 6 shows the intersection with the plane $v_r = 0$ of the trajectories of trapped plasma ions with $\mathcal{H}_i \approx 0.062$. Each color identifies an orbit of different initial condition. This Poincaré section has a couple of two-lobe structures around $\theta = 0$ and $\theta = \pi$ but, for clarity, only the two lobes around $\theta = 0$ are shown in Fig. 6. Unlike Fig. 3, which corresponds to a cylindrical probe, $p_\theta$ is not a constant of motion and a mix of regular and chaotic orbits appears. As highlighted in the inset of Fig. 6, there are Poincaré-Birkhoff chains and chaotic layers.

The appearance of chaotic orbits in phase space has a consequence in the structure of the distribution function. The boundary that separates trapped and non-trapped particles in the $\mathcal{H}_i - \zeta$ plane cannot be a smooth curve like the red line in Fig. 5 for cylindrical probes. For elliptical probes, such a boundary may have a fractal structure and the distribution function should be filamented in the velocity space. This feature was studied by considering in detail the ion distribution function at $(x, y) = (3.54, 0)$ and $\mathcal{H}_i \approx 0.062$. Its structure was computed with a high resolution for a small $\zeta$-range and the CN integrator. As shown in Fig. 7, we marked the corresponding $\zeta$-values used in the initial conditions with red, blue,

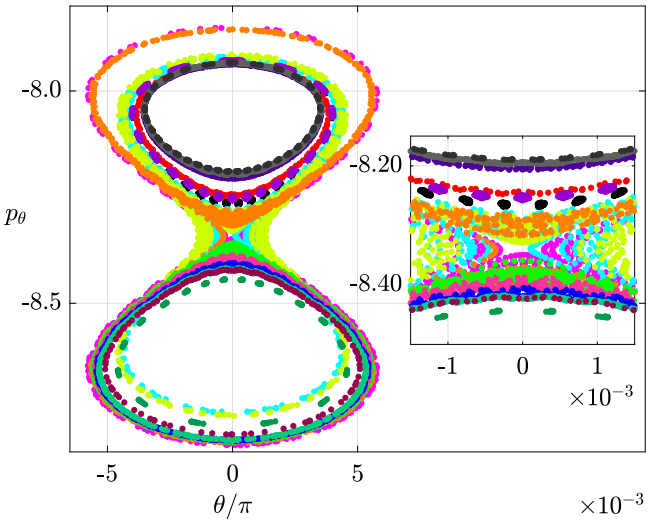


**Fig. 6.** Poincaré section ($p_r = 0$ plane) of trajectories of trapped ions. All trajectories have $\mathcal{H}_i \approx 0.062$, but different sets of $(r_0, \theta_0, \zeta_0)$, each one identified by a different color. (For interpretation of the colors in the figure(s), the reader is referred to the web version of this article.)

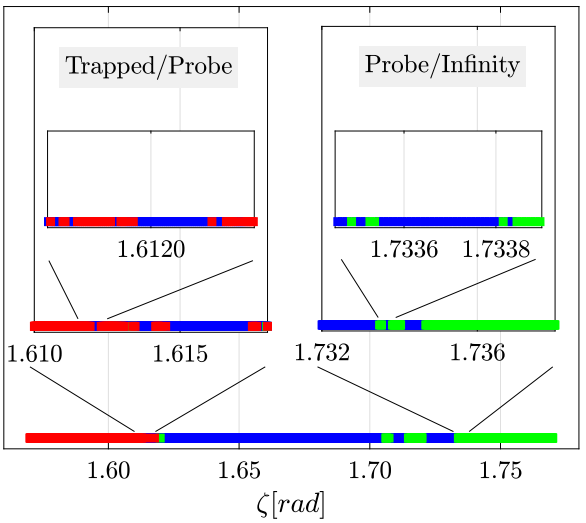


**Fig. 7.** Structure of the ion distribution function at $(x, y) = (3.54, 0)$ with $\mathcal{H}_i \approx 0.062$. Research data and post-processing scripts can be found at [dataset] [33]. (For interpretation of the colors in the figure(s), the reader is referred to the web version of this article.)

or green colors if the trajectories were trapped, hit the probe or reached the plasma boundary, respectively. The result for the range $1.57 \leq \zeta \leq 1.77$, and two details of smaller $\zeta$-ranges are shown. The boundary in the $\zeta$-axis that separates orbits that are trapped from the ones that hit the probe is not regular but exhibits a complex geometry. When looking at smaller scales (using a resolution 10 times bigger) in the $\zeta$-variable, a mix of the two types of orbits is observed. However, the distribution function around this boundary is smooth in our model because in both cases its value is set to zero. This is not the case for the boundary that separates probe-hitting orbits from the ones reaching infinity that also has a complex structure, as shown in Fig. 7 (right insets). In this case, the value of the ion distribution function is zero if the corresponding orbit reaches the probe and equal to the Maxwellian if it reaches infinity. Therefore, the distribution function is filamented and irregular.

## 5. Conclusions

This work discussed some limitations that are inherent to stationary Vlasov solvers based on backward Liouville methods. According to the numerical results provided by a novel Vlasov code applied to the analysis of 2-dimensional Langmuir probes with elliptical cross-sections, the following set of recommendations was found. Detailed studies of the particle dynamics around a cylindrical probe revealed that numerical errors break the conservation of physical invariants (energy and

angular momentum) unless specifically designed algorithms are used. Trapped particles are the most affected population. The main responsible for these errors is not the numerical integrator, but the algorithm that reconstructs the electric field along the particle orbits from the value of the electrostatic potential at the nodes of the mesh. For this reason, a structured mesh provides a better performance than an unstructured one in our study. Very detailed and accurate analysis requires the use of energy-conserving algorithms, like the Crank-Nicolson scheme.

The analysis of the orbits of the trapped particles in the self-consistent sheath of an elliptic probe revealed the presence of chaos. This feature, which is not related to the numerical algorithm, creates complex structures in the distribution function and the boundaries in velocity space that separates regions of different kinds of orbits are not smooth. The distribution function is filamented (fractal structure). For this reason, the integrable or non-integrable character of a physical configuration should be also considered before developing a stationary Vlasov-Poisson solver based on a backward Liouville method. For integrable problems, like for instance a cylindrical probe, arc-length algorithms that just computes such boundaries instead of the distribution function at every point of a mesh in velocity space can save important computational resources. For non-integrable problems this approach is obviously discouraged and it is necessary to evaluate the distribution function at every point of the mesh in velocity space. The mesh acts as a filter that removes the fine structure of the distribution function. The filamentation can also explain the lack of convergence of stationary VP solvers observed in past works.

Previous conclusions are linked to the criterion to classify a particle orbit as trapped. In this work, an orbit was considered as trapped if the number of loops performed around the probe before hitting the boundaries of the computational domain was larger than a numerical parameter named $N_{tr}$. The optimal choice of $N_{tr}$ depends on both the physical configuration of the problem and the choice of the numerical integrator, and it requires a brief parametric study to tune its value. For integrable configurations, like a round probe, the boundary that separates trapped from non-trapped particle in phase space is smooth. If the chosen integrator conserves the energy, then $N_{tr}$ should be selected by increasing $N_{tr}$ in the parametric analysis until the local value of the density does not change. If the chosen integrator does not conserve the energy, then the situation is different. For a too small $N_{tr}$, particle trajectories that should connect with the outer boundary or the probe are classified incorrectly as trapped. On the contrary, if $N_{tr}$ is too large, numerical errors accumulated during the long integrations make trapped orbits incorrectly hit a boundary of the computational domain. The choice of $N_{tr}$ should be made according to such a trade-off analysis and keeping in mind that a high value of $N_{tr}$ increases the computational cost. For non-integrable configurations, the distribution function is filamented and the previously mentioned boundary in phase space is a fractal. Such a feature is physical (totally unrelated to the numerical algorithm). In this case, it is recommended to follow a similar procedure to the one described for the numerical integrator that does not conserve the energy applied to integrable configurations. Again, a very large value of $N_{tr}$ will overestimate the plasma density. This is true even if an energy-conserving numerical integrator is used because a chaotic mixing of trapped and non-trapped orbits exists in phase space. For all the cases, a test case for benchmarking, like a cylindrical probe in our case, is helpful to make decisions.

Despite the discussed limitations, stationary Vlasov-Poisson solvers based on a backward Liouville method remain a valuable tools for the investigation of Langmuir and emissive probes operating in a wide range of conditions because they provide a kinetic description without any statistical error. In most cases, the studies are mainly focused on the collected and emitted current and the structure of the electrostatic potential. For this reason, the FEM-RK solver combined with an unstructured mesh can be an appropriate choice to study probes with complex geometries (beyond cylinders and ellipses), because it finds the macroscopic quantities of interest with a reasonable accuracy and can handle any geometry of the probe. However, as shown in this work, the FDM-CN solver with structured mesh should be used to carry out detailed and fine analysis of kinetic features.

## CRediT authorship contribution statement

**L. Chiabó:** Data curation, Formal analysis, Investigation, Software, Validation, Visualization, Writing – original draft. **G. Sánchez-Arriaga:** Conceptualization, Formal analysis, Funding acquisition, Methodology, Project administration, Resources, Supervision, Writing – review & editing.

## Declaration of competing interest

The authors declare that they have no known competing financial interests or personal relationships that could have appeared to influence the work reported in this paper.

## Acknowledgements

This work was supported by the European Union's Horizon 2020 Research and Innovation Programme under grant agreement No 828902 (E.T.PACK project). GSA work is supported by the Ministerio de Ciencia, Innovación of Spain under the Grant RYC-2014-15357. The authors thank the Reviewers for their valuable comments and suggestions about the use of energy-conserving numerical integrators.

## Appendix A. Numerical algorithms

### A.1. Meshes and coordinates

The FEM-RK solver uses Cartesian coordinates $(x, y)$, and an unstructured mesh with $N$ nodes. The computational domain is bounded by the probe ($\Gamma$) and a circumference of radio $r_{max}$ ($\Omega_{max}$). As shown in Fig. 2 (left panel), a higher density of nodes is placed close to the probe.

The FDM-RK and FDM-CN solvers work with two types of coordinates. For cylindrical probes, they use the cylindrical coordinates $(\chi^1, \chi^2) = (r, \theta)$ defined by

$$x(r,\theta) = r\cos\theta \quad y(r,\theta) = r\sin\theta \tag{A.1}$$

and the computational box is $r \in [r_p, r_{max}] \times \theta \in [0, \pi/2]$. For elliptic probes, the solvers use the elliptic coordinates $(\chi^1, \chi^2) = (\xi, \eta)$

$$x(\xi,\eta) = c_p \cosh\xi \cdot \cos\eta \quad y(\xi,\eta) = c_p \sinh\xi \cdot \sin\eta \tag{A.2}$$

with $c_p \equiv e_p r_p/\sqrt{1-e_p^2}$. The lines $\xi = constant$ and $\eta = constant$ represent confocal ellipses and hyperbolae, respectively. The computational domain is $\xi \in [\xi_p, \xi_{max}] \times \eta \in [0, \pi/2]$. For both geometries, we introduce an uniform mesh with $N_{\chi^1} \times N_{\chi^2}$ nodes of coordinates $\chi_i^1 = \chi_p^1 + (i-1)\Delta\chi^1$ and $\chi_j^2 = (j-1)\Delta\chi^2$ with $i = 1, \ldots, N_{\chi^1}$ and $j = 1, \ldots N_{\chi^2}$, $\Delta\chi^1 \equiv (\chi_{max}^1 - \chi_p^1)/(N_{\chi^1} - 1)$, and $\Delta\chi^2 \equiv \pi/2(N_{\chi^2} - 1)$. For later use, we also define now the contravariant base vectors $\boldsymbol{a}^k = \nabla\chi^k$ and the covariant base vectors $\boldsymbol{a}_k = \partial\boldsymbol{r}/\partial\chi^k$ with $k = 1,\ 2$.

### A.2. Poisson solvers

Ref. [26] explains in very detail the procedure to compute matrix $\bar{\boldsymbol{A}}$ and vector $\boldsymbol{\phi}_{BC}$ in Eq. (7) for the finite element-based Poisson solver used for the unstructured mesh. Regarding the structured meshes, Poisson equation in cylindrical and elliptic coordinates reads

$$\frac{\partial^2\phi}{\partial r^2} + \frac{1}{r}\frac{\partial\phi}{\partial r} + \frac{1}{r^2}\frac{\partial^2\phi}{\partial\theta^2} = -\rho \tag{A.3}$$

$$\frac{1}{c_p^2\left(\sinh^2\xi + \sin^2\eta\right)}\left(\frac{\partial^2\phi}{\partial\xi^2} + \frac{\partial^2\phi}{\partial\eta^2}\right) = -\rho. \tag{A.4}$$

In both cases we used the following centered finite difference scheme

$$\left.\frac{\partial\phi}{\partial r}\right|_{i,j} \approx \frac{\phi_{i+1,j} - \phi_{i-1,j}}{2\Delta r}, \tag{A.5}$$

$$\left.\frac{\partial^2\phi}{\partial r^2}\right|_{i,j} \approx \frac{\phi_{i+1,j} - 2\phi_{i,j} + \phi_{i-1,j}}{\Delta r^2}, \tag{A.6}$$

and similar formulae for $\partial^2\phi/\partial\theta^2$, $\partial^2\phi/\partial\xi^2$, and $\partial^2\phi/\partial\eta^2$. In Eqs. (A.5)-(A.6) the sub-indexes $i$ and $j$ means that the variable is evaluated at the node $(\chi_i^1, \chi_j^2)$. When constructing matrix $\bar{\boldsymbol{A}}$ from Eqs. (A.3)-(A.4) and (A.5)-(A.6) index $i$ runs from 2 to $N_{\chi^1}$. The value of the potential at $i = 1$ is known ($\phi_{1,j} = \phi_p$) and this contribution appears in vector $\boldsymbol{\phi}_{BC}$. At $i = N_{\chi^1}$ one should use that, for $r_{max}$ (or $\xi_{max}$), the potential decays as [26]

$$\phi \sim A_0\frac{r_{max}}{r} + \sum_{n==1}^{N_{modes}}\left(\frac{r_{max}}{r}\right)^{n+1}(A_n\cos\theta + B_n\sin\theta), \tag{A.7}$$

with $N_{modes}$ a high enough integer and the explicit formulae of coefficients $A_0$, $A_n$ and $B_n$ given in Ref. [26]. Regarding $\chi^2$, the following boundary conditions should be used $\phi_{i,-1} = \phi_{i,2}$ and $\phi_{i,N_{\chi^2}+1} = \phi_{i,N_{\chi^2}-1}$.

### A.3. Numerical integrators

The work considered three numerical integrators. The first two are an explicit and time-variable Runge-Kutta (RK) algorithm [30] and a second-order (symplectic) LeapFrog (LF) scheme [30]. These were applied to unstructured (structured) meshes in the FEM-RK and FEM-LF (FDM-RK and FDM-LF) solvers (see Fig. 4). For every time step, the reconstruction of the electric field $\boldsymbol{E}$ from the values of the electrostatic potential at the nodes depends on the type of mesh. For the unstructured mesh, we first calculate at every node the best (in the least-square sense [30]) second order polynomial fitting $\phi(x, y)$ in

the neighborhood of the node. According to Eq. (3), the electric field at the node is found by computing the gradient of the polynomial analytically. Once its values are known at all the nodes, the electric field is found at any point during the integration by using a natural neighbor interpolation algorithm [32]. For the structured mesh, the values of the electric field at the nodes are evaluated from Eq. (3) with a second-order centered finite difference scheme and the integrator uses bilinear interpolation [30] for evaluating the value of the field along the trajectory.

The third integrator is an implicit Crank-Nicolson scheme used in particle-in-cell codes [38,39,31]. It is a hybrid algorithm that propagates velocities in Cartesian space and position in logical curvilinear coordinates. Equations (8)-(9) read

$$\dot{\chi}^k = \boldsymbol{v}\cdot\boldsymbol{a}^k \quad k=1,2 \tag{A.8a}$$

$$\dot{\boldsymbol{v}} = \frac{e_\alpha}{\delta_\alpha}\boldsymbol{E}. \tag{A.8b}$$

If we use superscript $\nu$ and $\nu+1$ to denote the values of the variables at $\tau=\tau_\nu$ and $\tau=\tau_\nu+\Delta\tau$, the discrete forms of Eqs. (A.8) using the implicit Crank-Nicolson scheme are

$$\frac{\chi^{k,\nu+1}-\chi^{k,\nu}}{\Delta\tau} = \boldsymbol{v}^{\nu+1/2}\cdot\boldsymbol{a}^{k,\nu+1/2} \quad k=1,2 \tag{A.9a}$$

$$\frac{\boldsymbol{v}^{\nu+1}-\boldsymbol{v}^{\nu}}{\Delta\tau} = \frac{e_\alpha}{\delta_\alpha}E_k^{\nu+1/2}\boldsymbol{a}^{k,\nu+1/2}, \tag{A.9b}$$

where $\boldsymbol{v}^{\nu+1/2}=(\boldsymbol{v}^{\nu+1}+\boldsymbol{v}^{\nu})/2$, $\boldsymbol{a}^{k,\nu+1/2}=(\boldsymbol{a}^{k,\nu+1}+\boldsymbol{a}^{k,\nu})/2$, and we used Einstein summation convention. The covariant electric field components at the RHS of Eq. (A.9b) are $E_k=\boldsymbol{E}\cdot\boldsymbol{a}_k$ and they are computed following Ref. [31], which is based on B-spline functions and guarantees the conservation of the energy. We do not repeat here the full procedure of Ref. [31], but highlight that the electrostatic potential does not depend on time in our problem and the boundary conditions of $\phi$ are not periodic. This latter case was considered in Ref. [40]. Stationarity simplifies the calculation of $E_k^{\nu+1/2}$, while boundary conditions were imposed by adding ghost cells to our computational domain (inside $\Gamma$ and outside $\Omega_{max}$). For each value of $\chi^2$, the value of $\phi(\chi_1^1-\Delta\chi^1,\chi^2)$ and $\phi(\chi_{N_{\chi^1}}^1+\Delta\chi^1,\chi^2)$ at these ghost cells are computed through quadratic extrapolation in $\chi^1$.

## Appendix B. Supplementary material

Research data and post-processing files for Fig. 5 and Fig. 7 are available at [dataset] [33].
Supplementary material related to this article can be found online at https://doi.org/10.1016/j.jcp.2021.110366.

## References


[1] A. Ghizzo, F. Huot, P. Bertrand, A non-periodic 2d semi-Lagrangian Vlasov code for laser–plasma interaction on parallel computer, J. Comput. Phys. 186 (1) (2003) 47–69, https://doi.org/10.1016/S0021-9991(03)00010-X.
[2] G. Lehmann, Efficient semi-Lagrangian Vlasov-Maxwell simulations of high order harmonic generation from relativistic laser-plasma interactions, Commun. Comput. Phys. 20 (3) (2016) 583–602, https://doi.org/10.4208/cicp.OA-2015-0019.
[3] T. Umeda, J.-i. Miwa, Y. Matsumoto, T.K.M. Nakamura, K. Togano, K. Fukazawa, I. Shinohara, Full electromagnetic Vlasov code simulation of the Kelvin–Helmholtz instability, Phys. Plasmas 17 (5) (2010) 052311, https://doi.org/10.1063/1.3422547.
[4] E. Camporeale, G. Delzanno, B. Bergen, J. Moulton, On the velocity space discretization for the Vlasov–Poisson system: comparison between implicit Hermite spectral and particle-in-cell methods, Comput. Phys. Commun. 198 (2016) 47–58, https://doi.org/10.1016/j.cpc.2015.09.002.
[5] M. Shoucri, H. Gerhauser, K.H. Finken, Oscillations of the collisionless sheath at grazing incidence of the magnetic field, Phys. Plasmas 16 (10) (2009), https://doi.org/10.1063/1.3250290.
[6] G. Sanchez-Arriaga, J. Zhou, E. Ahedo, M. Martinez-Sanchez, J.J. Ramos, Kinetic features and non-stationary electron trapping in paraxial magnetic nozzles, Plasma Sources Sci. Technol. 27 (3) (2018), https://doi.org/10.1088/1361-6595/aaad7f.
[7] A.J. Klimas, A method for overcoming the velocity space filamentation problem in collisionless plasma model solutions, J. Comput. Phys. 68 (1) (1987) 202–226, https://doi.org/10.1016/0021-9991(87)90052-0.
[8] J. Candy, R. Waltz, An Eulerian gyrokinetic-Maxwell solver, J. Comput. Phys. 186 (2) (2003) 545–581, https://doi.org/10.1016/S0021-9991(03)00079-2.
[9] M. Shoucri, Eulerian codes for the numerical solution of the Vlasov equation, Commun. Nonlinear Sci. Numer. Simul. 13 (1) (2008) 174–182, https://doi.org/10.1016/j.cnsns.2007.04.004.
[10] M. Shoucri (Ed.), Eulerian Codes for the Numerical Solution of the Kinetic Equations of Plasmas, Nova Science Publishers Inc., 2010.
[11] C. Cheng, G. Knorr, The integration of the Vlasov equation in configuration space, J. Comput. Phys. 22 (3) (1976) 330–351, https://doi.org/10.1016/0021-9991(76)90053-X.
[12] F. Filbet, E. Sonnendrücker, P. Bertrand, Conservative numerical schemes for the Vlasov equation, J. Comput. Phys. 172 (1) (2001) 166–187, https://doi.org/10.1006/jcph.2001.6818.
[13] J. Büchner, Advanced Methods for Space Simulations, TERRAPUB, Tokyo, 2007.
[14] F. Filbet, E. Sonnendrücker, Comparison of Eulerian Vlasov solvers, Comput. Phys. Commun. 150 (3) (2003) 247–266, https://doi.org/10.1016/S0010-4655(02)00694-X.
[15] L. Einkemmer, A. Ostermann, A strategy to suppress recurrence in grid-based Vlasov solvers, Eur. Phys. J. D 68 (7) (2014) 197, https://doi.org/10.1140/epjd/e2014-50058-x.
[16] A.F. Viñas, A.J. Klimas, Flux-balance Vlasov simulation with filamentation filtration, J. Comput. Phys. 375 (2018) 983–1004, https://doi.org/10.1016/j.jcp.2018.09.014.

[17] L. Garcia, J. Goedert, Numerical investigation of the influence of vacuum space on plasma sheath dynamics, Phys. Lett. A 255 (4) (1999) 311–317, https://doi.org/10.1016/S0375-9601(99)00179-6.
[18] M. Shoucri, H. Gerhauser, K.-H. Finken, Study of the generation of a charge separation and electric field at a plasma edge using Eulerian Vlasov codes in cylindrical geometry, Comput. Phys. Commun. 164 (1) (2004) 138–149, https://doi.org/10.1016/j.cpc.2004.06.022.
[19] G. Sánchez-Arriaga, A direct Vlasov code to study the non-stationary current collection by a cylindrical Langmuir probe, Phys. Plasmas 20 (1) (2013) 013504, https://doi.org/10.1063/1.4774398.
[20] G. Sánchez-Arriaga, D. Pastor-Moreno, Direct Vlasov simulations of electron-attracting cylindrical Langmuir probes in flowing plasmas, Phys. Plasmas 21 (7) (2014) 073504, https://doi.org/10.1063/1.4889732.
[21] H.M. Mott-Smith, I. Langmuir, The theory of collectors in gaseous discharges, Phys. Rev. 28 (1926) 727–763, https://doi.org/10.1103/PhysRev.28.727.
[22] S.H. Lam, Unified theory for the Langmuir probe in a collisionless plasma, Phys. Fluids 8 (1) (1965) 73–87, https://doi.org/10.1063/1.1761103.
[23] I.B. Bernstein, I.N. Rabinowitz, Theory of electrostatic probes in a low-density plasma, Phys. Fluids 2 (2) (1959) 112–121, https://doi.org/10.1063/1.1705900.
[24] J.G. Laframboise, Theory of Spherical and Cylindrical Langmuir Probes in a Collisionless, Maxwellian Plasma at Rest, PhD thesis, University of Toronto, Canada, 1966.
[25] J.R. Sanmartín, R.D. Estes, The orbital-motion-limited regime of cylindrical Langmuir probes, Phys. Plasmas 6 (1) (1999) 395–405, https://doi.org/10.1063/1.873293.
[26] E. Choiniere, Theory and experimental evaluation of a consistent steady-state kinetic model for 2-d conductive structures in ionospheric plasmas with application to bare electrodynamic tethers in space, 2004.
[27] X. Chen, G. Sanchez-Arriaga, Orbital motion theory and operational regimes for cylindrical emissive probes, Phys. Plasmas 24 (2) (2017) 023504, https://doi.org/10.1063/1.4975088.
[28] J.C. McMahon, G.Z. Xu, J.G. Laframboise, The effect of ion drift on the sheath, presheath, and ion-current collection for cylinders in a collisionless plasma, Phys. Plasmas 12 (6) (2005) 062109, https://doi.org/10.1063/1.1924392.
[29] R. Marchand, Test-particle simulation of space plasmas, Commun. Comput. Phys. 8 (3) (2010) 471–483, https://doi.org/10.4208/cicp.201009.280110a.
[30] W.H. Press, et al., Numerical recipes in FORTRAN, in: The Art of Scientific Computing, 2nd ed., Cambridge University Press, 1992.
[31] L. Chacón, G. Chen, A curvilinear, fully implicit, conservative electromagnetic PIC algorithm in multiple dimensions, J. Comput. Phys. 316 (2016) 578–579, https://doi.org/10.1016/j.jcp.2016.03.070.
[32] R. Sibson, Interpolating Multivariate Data, John Wiley, Chichester, 1981.
[33] L. Chiabó, G. Sánchez-Arriaga, Limitations of stationary Vlasov-Poisson solvers in probe theory, https://doi.org/10.21950/PNYKF5, 2020, e-cienciaDatos, V1.
[34] V. Pletnev, J.G. Laframboise, Current collection by a cylindrical probe in a partly ionized, collisional plasma, Phys. Plasmas 13 (7) (2006) 073503, https://doi.org/10.1063/1.2208620.
[35] M. Martinez-Sanchez, J. Navarro-Cavallé, E. Ahedo, Electron cooling and finite potential drop in a magnetized plasma expansion, Phys. Plasmas 22 (5) (2015) 053501, https://doi.org/10.1063/1.4919627.
[36] J.G. Laframboise, L.W. Parker, Probe design for orbit-limited current collection, Phys. Fluids 16 (5) (1973) 629–636, https://doi.org/10.1063/1.1694398.
[37] J.R. Sanmartín, CNES-space technology course: prevention of risks related to spacecraft charging, in: J.P. Catani (Ed.), Cepadus, Toulouse, France, 2002.
[38] L. Chacón, G. Chen, D.C. Barnes, A charge- and energy-conserving implicit, electrostatic particle-in-cell algorithm on mapped computational meshes, J. Comput. Phys. 233 (2013) 1–9, https://doi.org/10.1016/j.jcp.2012.07.042.
[39] G.L. Delzanno, et al., CPIC: a curvilinear particle-in-cell code for plasma–material interaction studies, IEEE Trans. Plasma Sci. 41 (2013) (Dec. 2013) 3577–3587, https://doi.org/10.1109/TPS.2013.2290060.
[40] L. Chacón, G. Chen, Energy-conserving perfect-conductor boundary conditions for an implicit, curvilinear Darwin particle-in-cell algorithm, J. Comput. Phys. 391 (2019) 216–225, https://doi.org/10.1016/j.jcp.2019.04.032.